Journal of Colloid and Interface Science 613 (2022) 207–217

Contents lists available at ScienceDirect

Journal of Colloid and Interface Science

journal homepage: www.elsevier.com/locate/jcis

Modulating the chiral nanoarchitecture of cellulose nanocrystals through interaction with salts and polymer

Maoqi Lin [a], Vikram Singh Raghuwanshi [a], Christine Browne [a], George P Simon [b], Gil Garnier [a,*]

[a] Bioresource Processing Research Institute of Australia (BioPRIA), Department of Chemical & Biological Engineering, Monash University, Clayton, VIC 3800, Australia
[b] Department of Materials Science and Engineering, Monash University, Clayton, VIC 3800, Australia

GRAPHICAL ABSTRACT

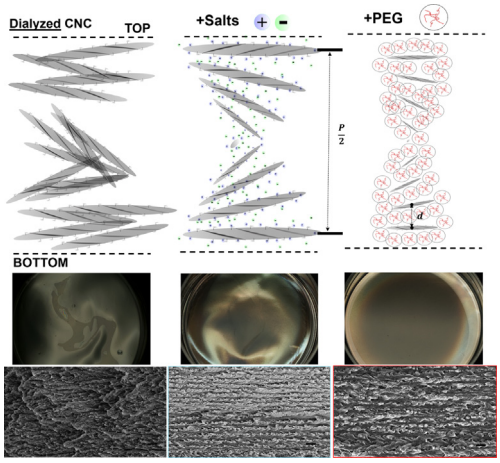

ARTICLE INFO

Article history:
Received 10 November 2021
Revised 20 December 2021
Accepted 28 December 2021
Available online 30 December 2021

Keywords:
Cellulose Nanocrystal (CNC)
Inorganic salts
Polyethylene glycol (PEG)
Chirality
Achiral and chiral nematic phase
Self-assembly

ABSTRACT

Hypothesis: The conditions to allow self-assembly of cellulose nanocrystal (CNC) suspensions into chiral nematic structures are based on aspect ratio, surface charge density and a balance between repulsive and attractive forces between CNC particles.
Experiments: Three types of systems were characterized in suspensions and subsequently in their solid dried films: 1) neat water dialyzed CNC, 2) CNC combined with polyethylene glycol(PEG) (CNC/PEG), and 3) CNC with added salt (CNC/Salt). All suspensions were characterized by polarized optical microscope (POM) and small angle X-ray scattering (SAXS), while the resultant dried films were analyzed by reflectance spectrometer, scanning electron microscope (SEM) and SAXS.
Findings: The presence of chiral nematic (CN*) structures was not observed in dialyzed aqueous suspensions of CNC during water evaporation. By introducing salts or a non-adsorbing polymer, chirality was apparent in both suspensions and films. The interaxial angle between CNC rods increased when the suspensions of CNC/PEG and CNC/salt were dried to solid films. The angle was found to be dependent on both species of ions and ionic strength, while the inter-particle distance was only related to the salt concentration, as explained in terms of interaction energies. The CNC suspensions/film chirality can be modulated by controlling the colloidal forces.

* Corresponding author.
E-mail address: Gil.Garnier@monash.edu (G. Garnier).

https://doi.org/10.1016/j.jcis.2021.12.182
0021-9797/

1. Introduction

The self-assembly of biopolymers colloids to produce colors at selective wavelengths of light by reflection and transmission is compelling [1,2]. During this self-assembly process, many competing and interacting factors determine the structures of the biopolymer composites, from the nanoscale to the microscale. Understanding and controlling this process is desirable to engineering applications, such as sustainable photonic materials.

Cellulose nanocrystals (CNC) are rod-like semi-crystalline colloidal particles, chemically extracted from a cellulosic source such as wood pulp and cotton [3]. CNCs are certainly the most abundant organic nanoparticles. The common refining process to produce them involves a sulfuric acid hydrolysis which dissolves the amorphous sections of cellulose binding the crystals, endowing the final CNC with its surface charge. This characteristic of high surface charge combined with high hydroxyl concentration makes CNC very dispersible in water and provides great potential for further functionalization [4,5] and subsequent photonic applications [2,6]. Sulfonated CNC aqueous suspensions show a lyotropic behaviour and produce stronger birefringence with increasing CNC concentration. There is a threshold for CNC suspension stability defined by zeta potential. When the zeta potential is less than a threshold of around – 25 mV, CNCs can self-assemble from an isotropic phase into a chiral nematic (CN*) structure, also known as "cholesteric" structure [7–12]. As the CNC surface charge decreases, the suspension stability is lost and CNCs agglomerate during evaporation. Desulfonated CNCs and HCl-hydrolyzed CNCs have a low surface charge and do not demonstrate significant liquid crystalline properties in their aqueous suspensions [13]. In this case, CNCs become randomly packed and aggregate without attaining a CN* structure. Electrostatic repulsions between CNC rods provide colloidal stability and help achieve and retain CN* structures during the self-assembly process [14].

It has been shown that CNC films from suspension-casting form left-handed CN* structures which polarize incident light and reflect a left-handed light [15]. The wavelength (λ) of the reflected light follows the Bragg's law:

$$\lambda = n_{av} \cdot \boldsymbol{P} \cdot cos\theta \quad (1)$$

where n_{av} is the average refractive index of local helical structure, $\boldsymbol{P}$ is the pitch dimension in the CN* structure and θ is the angle of light incidence. Adding electrolytes and polymers into the CNC suspension alters not only the wavelength of reflected light between ultraviolet (UV) and near infrared (NIR), but also the uniformity of color at the macroscopic scale. If the alignments of all CNC microdomains are not perpendicular to the surface of the dried film, the homogeneity of structure is disrupted and so is the uniformity of color [16,17].

Adding electrolytes or increasing ionic strength reduces the dimension of the pitch ($\boldsymbol{P}$) and causes the blue shift of the reflected light [8,18–20]. If the ionic strength exceeds a "critical aggregation concentration" (CAC) [18,21,22], the CNC suspension also loses its CN* liquid-crystalline properties as the CNC surface charge is screened. With regards to the ion-specific effect, Xue et al. [19] found little difference between H^+, Na^+ and K^+ cations when the concentration was below 2.5 mM. There is good agreement that the CAC [18,21–23] is dependent on the species and valency of ions for concentrations over 100 mM. Ion-specific effects appear to become significant as the concentration of electrolytes increases. Ragesh et al. [24] and Salvatore et al. [25] found that ion adsorption onto CNCs contributes to this ion-specific effect.

Adding polymers, on the other hand, can increase $\boldsymbol{P}$ and cause a red shift of the reflected light. The polymer chains embed between CNC rods and increase the CNC interaxial distance [26–29]. Key properties of the polymer such as molecular weight (MW) and the binding between polymer and CNC rods determine the degree of the increase in $\boldsymbol{P}$ per unit volume. For example, non-adsorbing polymers [8,30] or polymers of lower MW [31] show a depletion effect, where polymer chains are excluded between CNC rods. In this case, $\boldsymbol{P}$ decreases as the polymer concentration increases.

In this study, we investigate if electrostatic repulsive forces can be used to modulate CNC suspensions displaying the CN* phase and this hypothesis is proven and schematized in Fig. 1. We rely on screening with a series of selective electrolytes and a non-adsorbing polymer to attenuate the CNCs high surface charge. This is achieved either by adding a small quantity of salts, ranging from 10 $\mu mol/g_{CNC}$ to 100 $\mu mol/g_{CNC}$, or by adding 30 wt% of polyethylene glycols (PEG) into the CNC suspension. The Zeta-potential of the mixtures was measured to follow the reducing repulsion between CNC rods. The arrangement of CNC rods and resultant domains of isotropic, achiral nematic and CN* phases were monitored by polarized optical microscope (POM). To quantify the interaxial distance between neighboring (center-to-center distance) CNCs $\boldsymbol{d}$ of CN* phase, both suspensions and solid films were measured by small angle X-ray scattering (SAXS). The morphology of dried films obtained by scanning electron microscope (SEM) is used to quantify the pitch size $\boldsymbol{P}$. The corresponding interaxial angle $\boldsymbol{\varphi}$, defined by $\boldsymbol{d}$ and $\boldsymbol{P}$, was calculated for the different additives. CNC suspensions and films characteristics were analyzed as colloids, with the interaction energy of each systems related to the CNC superstructures achieved.

2. Method

2.1. Materials

CNC was purchased from the Maine University Process Development Centre (University of Maine, USA) and had been extracted from wood pulp using sulfuric acid hydrolysis. The CNC suspension was used as received. The original dry matter of the CNC suspension was 10.3 wt% containing 1.1 wt% sulfur with sodium counterions (Na^+). Polyethylene glycol (PEG) of MW equal to 900,000 Da was purchased from Dow® Chemistry. The molar mass was verified by size exclusion chromatography and is summarized in Table.S1 in Supporting Information (**S.I.**). Three salts, NaCl, KCl and $MgCl_2$ are traces metal basis grade (purity greater than 99.99%) purchased from Sigma Aldrich.

2.2. Preparation of suspensions

The gel-like commercial CNC product was diluted from 10.3 wt % to 2 wt% by the addition of Milli-Q water. PEG powder was dissolved in the Milli-Q water and reached the concentration of 0.8 wt%. The diluted CNC suspension and PEG solution were bagged separately in cellulose-made dialysis tubes which have 12,400 Da molecular weight cut off (MWCO) and dialyzed by Milli-Q water in ten-fold for three weeks, and the water was renewed daily. After dialysis, 5 mL of CNC suspension was blended with 5 mL of PEG solution and stirred at 750 rpm at 25 °C for 48 h. Salts were dissolved in Milli-Q water. The CNC suspension was produced by mixing designated concentrations of salt solutions to achieve 10, 50, and 100 $\mu mol/g_{CNC}$. All mixtures were shaken in an incubator at 200 rpm at 25 °C for 24 h. Pure CNC had the same concentration as the rest of suspensions before evaporation of water. The mixtures are labelled as CNC/PEG and CNC/Salt-Concentration. For example, CNC with 50 $\mu mol/g_{CNC}$ KCl is expressed as CNC/KCl50.

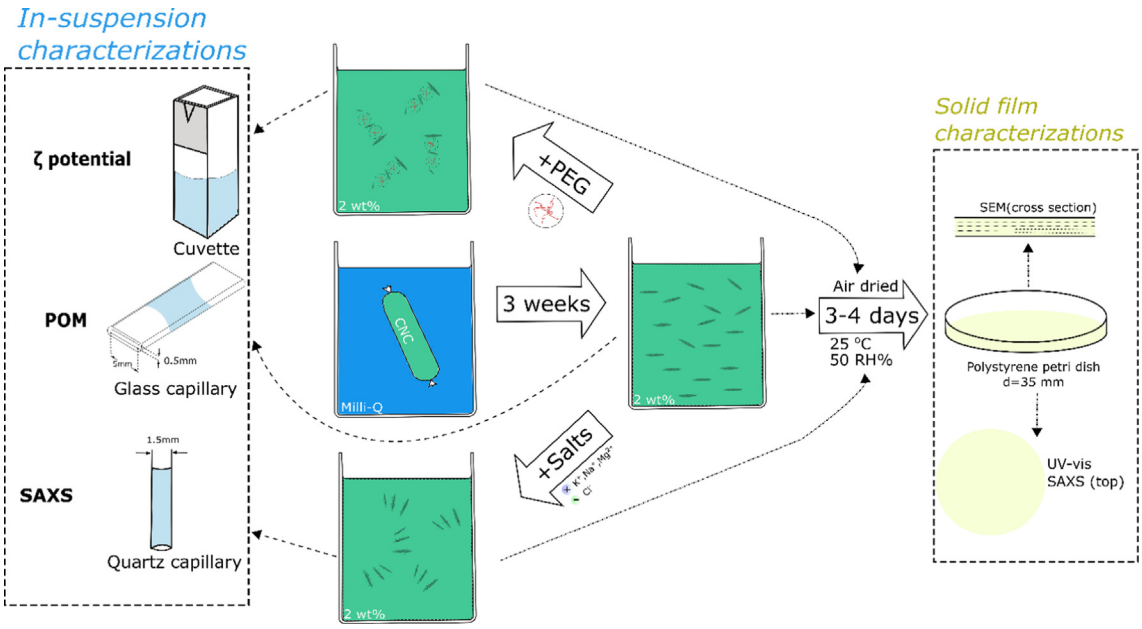

Fig. 1. Schematic of the experimental materials and techniques used.

2.3. Preparation of concentrated suspensions and solid film.

To concentrate samples to 4 wt% CNC, the suspensions were slowly dried in Eppendorf® tubes. To produce solid films, the suspensions were poured into polystyrene petri dishes. The whole drying process for both concentrated suspensions and solid film was in a dust-free environment at 25 °C, and 50% relative humidity for 4–6 days.

2.4. Characterization

Zeta potential measurements were obtained in triplicate by using a NanoBrook Omni at 25 °C. Data was presented based on Phase Electrophoretic Mobility method and the Smoluchowski equation [32].

Polarized optical microscopy (POM) is composed of Nikon Eclipse Ni-U body coupled with a pair of cross polarizers and a rotatable λ/4 waveplate was used to image suspension under the same illuminating condition and exposure time. The suspension was injected and retracted into a cuboid-like capillary under vacuum. The width of the capillary chamber is 500 μm, which is thick enough to reduce the possible spatial constraint on CNC structure when the solid content is below 5 wt% according to Cherpak et al [33]. The capillary was laid horizontally on the table overnight before imaging under POM to allow the structure to form into its stable state.

Small angle X-ray scattering (SAXS) technique was performed by using different instruments for suspensions and dried films. Suspension samples were measured at the SAXS/WAXS beamline of the Australian Synchrotron. Suspensions were filled into 1.5 mm thick quartz capillaries and measured in transmission mode by using the X-ray energy of 12 KeV. A Pilatus detector with the pixel size of 70 μm × 70 μm was used to collect the scattered X-rays. Glassy carbon and silver behenate are used to calibrate the scattering curves to the absolute units and scaling the q values. The data reduction and averaging of the scattering images was performed using the inhouse software Scatterbrain. Dried films were characterized at the lab-based Bruker N8 Horizons SAXS system equipped with a Cu-anode (wavelength = 1.5406 Å) radiation source, Vantec-500 2D detector and Montel multilayer optics. The operating power for the measurement in the transmission mode was 1 KW. The measurement was carried out under vacuum at room temperature. The data processing and analyses were performed using a Bruker DIFFRAC.SAXS program.

Scanning electron microscope (SEM) - FEI Magellan 400 FEGSEM was used for imaging cross-sections of the solid dried films. They were first cryo-fractured after being immersed in liquid nitrogen for 10 s. The fracture plane was coated with iridium (less than1 nm) to prevent charging during SEM imaging. The ImageJ software was used to measure the pitch size in each cross-sectional image.

Reflectance ultraviolet-visible analysis (R-UV-vis) was performed using an Ocean Optics HDX spectrometer with a DH-2000-L light source (200 nm – 1000 nm) and a UV–visible reflection probe (six illuminating fibers and one d = 400 μm read fiber), to study the reflectance intensity of the CN* structure in CNC solid films. The sample was placed horizontally on a black table and the probe was placed vertically at about 30 mm height above the sample with the measurement undertaken in a dark environment. The reference of reflectance measurement was a UV-enhanced aluminum mirror (Edmund Optics®, $R_{avg} > 85\%$).

3. Results

To study the chirality of CNC assembly, three system: i) neat, dialyzed CNC; ii) CNC with 900,000 Dalton PEG (CNC/PEG); iii) CNC added with salt (CNC/salt) - were investigated in the form of suspensions and their solid films. Zeta potential and POM measurements determined the properties of CNC assembly in suspension, whilst SEM and UV–vis was used to identify any pitch and chirality in the solid films. To study the interactions between CNC rods during the process of water evaporation, both suspensions and solid film were measured by SAXS.

3.1. CNC suspensions

A series of aqueous suspensions at 4 wt% CNC solid content were selected to study CNC assembly; this is for their potential to form a biphasic state that includes both the isotropic and the nematic phase at this CNC concentration [15]. The zeta potentials

Table 1
Summary of the zeta-potentials of all CNC suspensions (4 wt%) showing the effect of salt type and PEG. Salt concentration was fixed at 40 mM. PEG concentration was 1.7 wt%.

Samples	Neat CNC	CNC/PEG	CNC/KCl50	CNC/NaCl50	CNC/$MgCl_2$50
ζ potential (mV)	−69.8 ± 1.1	−52.7 ± 5.7	−49.1 ± 6.3	−49.1 ± 5.1	−32.3 ± 6.2

of all CNC suspensions were measured, and all exhibited strong negative values. Neat CNC suspensions possess the highest zeta potential, −69.8 mV, which is well less than the threshold for agglomeration of around −25 mV [7,8]. After incorporating PEG, the zeta potential increased in magnitude to −52.7 mV. Adding salts into CNC suspensions increases the zeta potential compared to the non-salt systems (shown in Table. 1). CNC/KCl50 and CNC/NaCl50 have similar zeta potentials, while CNC/$MgCl_2$50 has a much smaller absolute value. Nonetheless, all are less than the threshold for agglomeration and lead to stable colloidal suspensions.

POM images of the neat CNC, CNC/PEG, CNC/KCl50, CNC/NaCl50 and CNC/$MgCl_2$ suspensions are shown in Fig. 2. The major images in Fig. 2 were filtered by cross-polarizers in the microscope. The brightness and colors of these major images result from the anisotropy of the liquid crystalline structures. By filtering the incoming light *via* cross-polarizers in POM, the image of the isotropic phase was completely dark, while the image of the biphasic state combines both partially dark and bright sections. The presence of a CN* phase is demonstrated by the appearance of a "fingerprint" texture composed of the region of closely packed parallel lines observed by POM[34]. The gap between neighbor lines is commonly considered as half the dimension of the CN* pitch (***P/2***) [35,36]. The other way to demonstrate the existence of CN* phase is by viewing the contrast under a left-circular polarizer (LCP) and a right-circular polarizer (RCP) [35]. It is usually found that the CN* phase in CNC film is a left-handed structure[37] which only reflects LCP light and transmits RCP light. When LCP light polarized by CNC film passes through the LCP filter in microscope, a weaker signal is captured by camera, as compared to non-polarized light and the image generated on the screen is of a lower intensity.

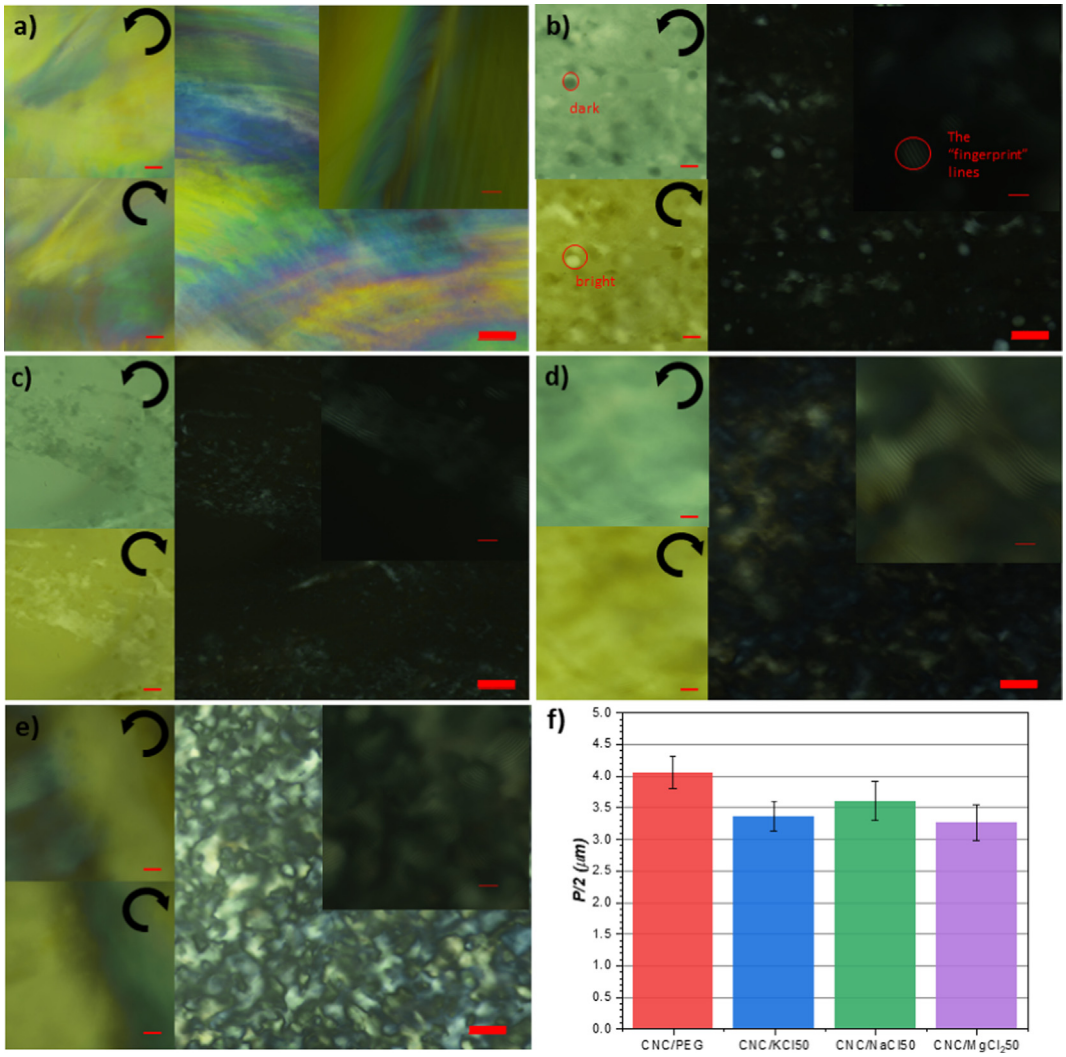

Fig. 2. A set of POM images of suspensions which are compacted in the rectangular capillaries including: a) CNC, b) CNC/PEG, c) CNC/KCl50, d) CNC/NaCl50, e) CNC/MgCl250 under the same illuminating condition. All suspensions have 4 wt% CNC solid content. The scale bar of each major image is 100 μm. The top-left corner is the image filtered by left-circular polarizer (LCP) and the bottom-left corner is the image filtered by right-circular polarizer (RCP), both with a scale bar of 50 μm. The top-right corner is a magnified image of the major image with a scale bar of 20 μm showing the fingerprint lines. f) summarizes pitch size for the various CNC suspensions by measuring the distance between the lines.

The major images of Fig. 2(a) representing the neat CNC suspension are the brightest and most colorful, indicating the largest volume of anisotropic phase of all suspensions. However, this anisotropic alignment does not include any CN* phases. There is no change in color and contrast when the filter was switched between LCP and RCP, suggesting little CN* structure in the neat CNC suspensions. The variety of colors in Fig. 2(a) mainly arises from the formation of a nematic structure without chirality, demonstrating the different orientation of CNCs aligned in a parallel fashion in small domains without "fingerprint" lines.

For the CNC/PEG suspension, the major image in Fig. 2(b) shows a reduced brightness and a reduced variety of colors compared with neat CNC suspensions, suggesting a biphasic state. By swapping the two circular polarizers, the dark areas become brighter and *vice versa*. In Fig. 2(b), the dark circle or ellipse areas under an LCP filter become brighter under an RCP filter. The "fingerprint" lines with approximate 4.0 μm gap appear in "bead-shaped" domains which proves the emergence of a CN* structure at 4 wt% CNC. Thus, both anisotropy and CN* structures can be observed in the CNC/PEG suspensions.

For the CNC/Salt systems, the biphasic state is also observed in the major image of Fig. 2(c)-(e). The bright domains in CNC/KCl50 are more scattered, with smaller areal size, than those in CNC/NaCl50. The major image of CNC/MgCl50 in Fig. 2(e) is brighter and more chromatic, indicating that most phases are CN* phase. A large bright green area on the left under the LCP filter and a mixture of dark green and blue areas under the RCP filter are observed in Fig. 2(e). It indicates that for CNC/MgCl50 (in Fig. 2(e)), the helix axes of CN* phase are oriented in a similar direction, and these independent areas expand and merge. The "fingerprint" lines were observed in all of Fig. 2(c)-(e). More specifically, the gap between these lines meaning ***P/2*** of CNC/KCl50, CNC/NaCl50 and CNC/$MgCl_2$ are measured as 3.36 μm, 3.60 μm and 3.25 μm, respectively.

SAXS was performed to determine the effect of PEG and salts on the interactions between CNC rods in the suspension form. The power-law slope β at smaller q value is shown in Fig. 3(a) and indi-

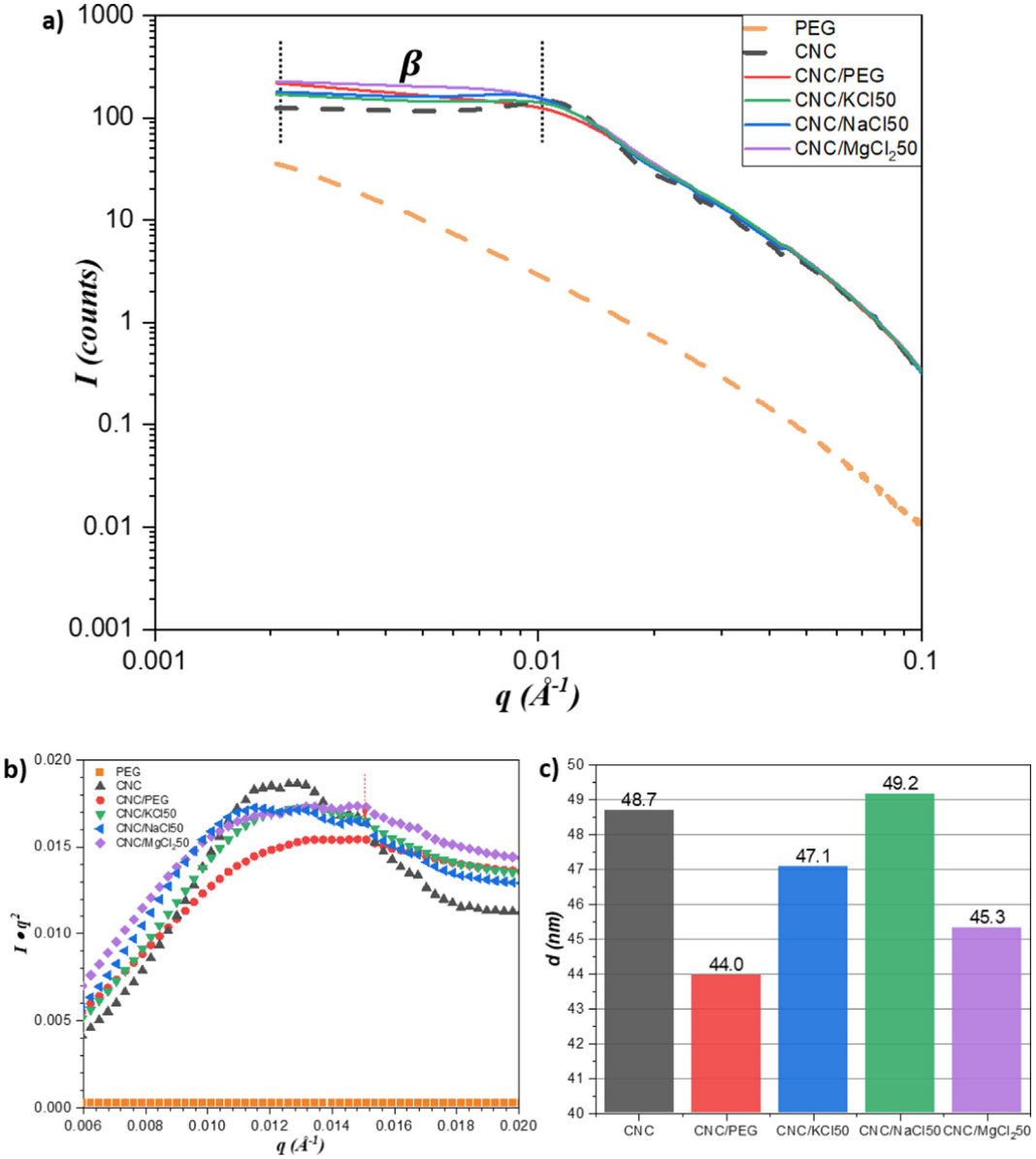

Fig. 3. Synchrotron SAXS data of CNC, CNC/PEG, CNC/KCl50, CNC/NaCl50 and CNC/MgCl250 with a CNC solid content of 4 wt%. a) is original plot after subtracting the background curve of Milli-Q water, and b) is corresponding Kratky plot. The round-dot line in b) indicates a sub-peak for CNC/NaCl50. c) The summary of ***d*** values determined by the equation $2\pi/q_{peak}$, where q_{peak} is the peak of each curve in Kratky plot.

cates that the formation of random agglomeration states[21,38,39] is less than 1. Since the smallest value of β for random agglomeration state is 2.1, as reported by Fanch et al.[21], β in this study reveals the self-assembly of CNC rods in an ordered manner. The corresponding Kratky plot of ($I \cdot q^2$ vs. q) from the SAXS curves in Fig. 3(b) provides information on the correlation peak at q_{peak} value between 0.01 and 0.02 Å^{-1}. The position of the correlation peaks is used for the calculation of interaxial distance (center-to-center) between rods d by the equation:

$$d = \frac{2\pi}{q_{peak}} \tag{2}$$

where q_{peak} is determined by fitting the curve with a Gaussian shape function and taken as the center point of fitting Gaussian curve, since it is a representative way to show the difference in d. The R^2 values of all data are greater than 0.99, which indicates very good overall fitting of the model with the original data.

PEG, as a non-ionic and non-absorbing polymer in CNC suspension, can also promote CNC rods to be closer, shifting d from 48.7 nm to 44.0 nm. The PEGs ability to decrease the CNC interaxial distance is as efficient as the addition of salt. Furthermore, the curve of CNC/PEG shows only one broadened peak at around 0.013 Å^{-1}, followed by a plateau instead of forming multi-peaks.

CNC/NaCl50 in suspension shows the greatest d, 49.2 nm, followed by the pristine CNC suspension, 48.7 nm. Multiple subpeaks of CNC/NaCl50 curve indicate multiple d values, while a single sharper peak of the neat CNC curve designates a more uniform interaxial distance between CNC rods. On average, the difference between CNC and CNC/NaCl50 is not significant and within error. d correlates with the species of ions, with CNC/$MgCl_2$50 showing the smallest d (45.3 nm) among the three CNC/salt systems.

3.2. Cellulose films cast from suspension

The different CNC suspensions were air-dried into solid films under ambient conditions. The optical and structural properties of the films were quantified by both color measurement based on reflectance UV–vis, and SEM imaging of the cross-section. For neat CNC, no iridescent color is observed, as shown in Fig. 4(a). Its UV–vis spectrum shows a weak and similar reflection intensity

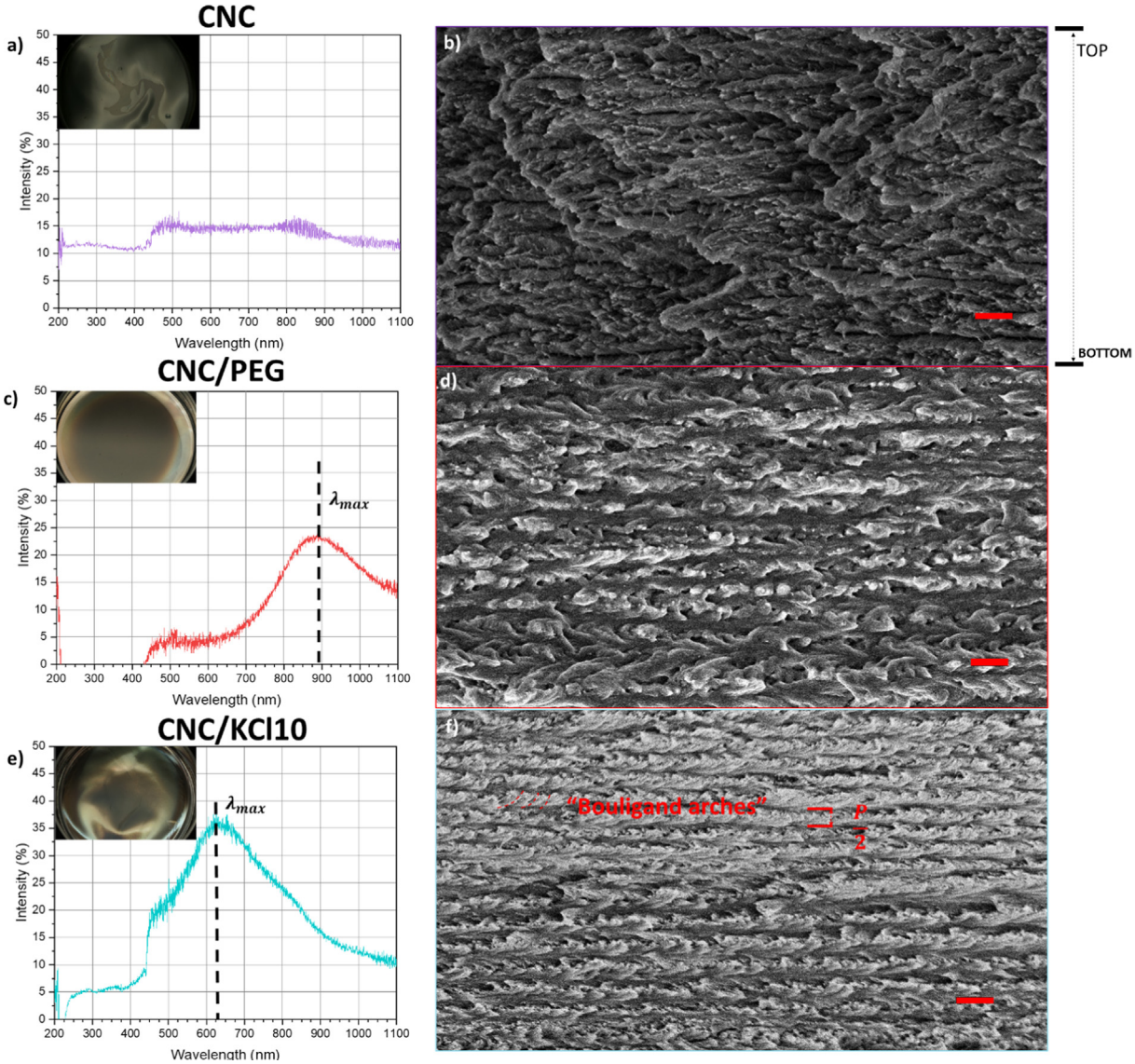

Fig. 4. Photonic properties and SEM structure of a-b) a neat CNC film, c-d) a CNC/PEG and e-f) a CNC/KCl10 film. a), c) and e) are spectra measured by reflectance UV–vis (R-UV–vis) accompanied with macro photos. b), d) and f) are SEM images of the cross-section of the film from top surface to bottom surface with 500 nm scale bars.

across the visible region from 450 nm to 850 nm. From the SEM images in Fig. 4(b), the clusters of CNCs stack on each other and pack into a laminated structure with high irregularity.

For the CNC/PEG systems after evaporation, the film shows a dark red color in Fig. 4(c) and the corresponding UV–vis shows a relatively sharp peak at 888 nm, as compared to the neat CNC film. The periodicity can be seen from the SEM image in Fig. 4(d). The dimension of ***P/2*** is measured to be around 255 nm. The morphology is of a CN* structure which is less defined, where the boundary of each period is less clear than for CNC/KCl10 in Fig. 4(f).

For the CNC/salts systems (Fig. 4(e)), the peak in UV–vis of CNC/KCl10 predominates and is sharper than that of the neat CNC. In Fig. 4(f), CN* phases are more structured and uniform. Each layer can be clearly distinguished as half a period representing ***P/2*** which is 239 nm. Each layer also contains "Bouligand arches", a further indicator of CN* phase in solid film[40]. The orientation of the localized helixes in the samples with salt additives is almost normal to the film surface.

As higher concentrations of salts from 10 μmol/g_{CNC} to 100 μmol/g_{CNC} were mixed with the CNCs, the thickness of layers

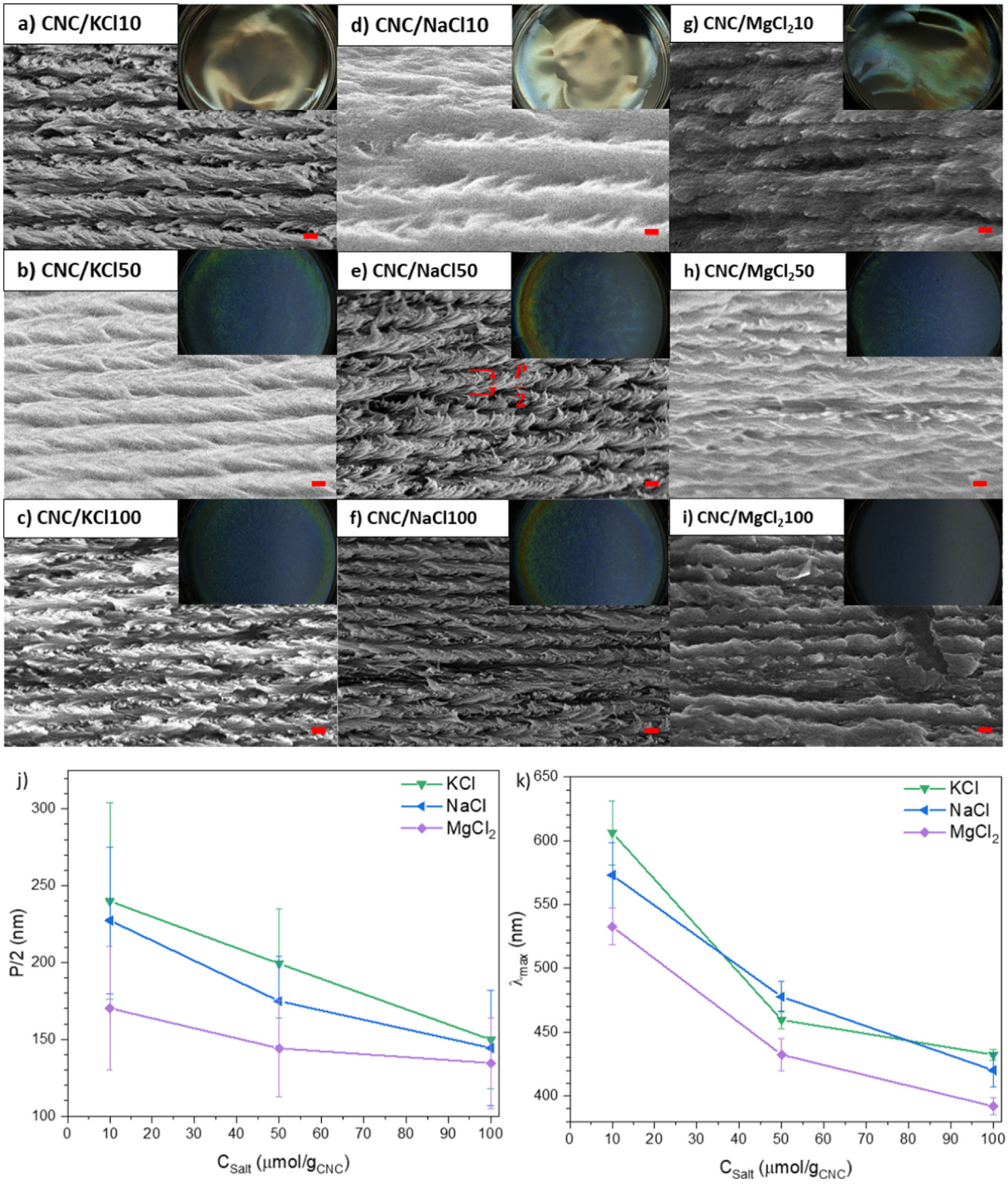

Fig. 5. Photonic properties and SEM structure of CNC/salts in terms of salt concentration ranging from 10 μmol/g_CNC to 100 μmol/g_CNC . a-i) are SEM images accompanied with macro photos. Scale bars in all SEM images are 100 nm. j-k) are the summary of the wavelength of half-pitch **P/2** and maximum intensity λ_{max} respectively.

became more homogeneous, with a smaller error for each point in Fig. 5(j). A higher concentration of salts results in a decrease of half pitch ***P/2*** corresponding to a blue shift of iridescent color with a smaller λ_{max}. These phenomena are consistent with previous work[41,42]. The color is shown to be more uniform across the film, as shown in Fig. 5(a-i). CNC films incorporating monovalent salts have larger decrement, $\Delta P/2$ and $\Delta\lambda_{max}$, as the salt concentration increases. Incorporating $MgCl_2$ into CNCs results in a blue-shift color of film, from 532.6 nm to 391.9 nm, as compared to the other salts. In addition, the appearance of CNC/$MgCl_2$100 in Fig. 5(i) is less colorful.

SAXS was performed on the dried CNC films to determine the interaxial distance between rods ***d*** from the correlation peak. From Fig. 6(b), the graph of the neat CNC dried film does not exhibit any significant sharp peak, but rather a turning point around 0.14 $Å^{-1}$ where the slope of curve suddenly changes. The value of ***d*** at this turning point is calculated using Eq.(2) to be 4.4 nm, which is very similar to the diameter of the CNC rods. In comparison, the CNC/PEG system shows a main peak at ***q*** values of around 0.07 $Å^{-1}$. CNC/Salts have much broader peaks between 0.10 and 0.11 $Å^{-1}$, as clearly seen in Fig. 6(c). Their corresponding values of ***d*** are summarized in Fig. 6(d). CNC/PEG has the largest value of ***d*** at 9.2 nm, while the ***d*** s of CNC/NaCl50, CNC/KCl50 and CNC/$MgCl_2$50 are all close to 6.0 nm.

4. Discussion

From these measurements, we propose that neither the neat CNC suspension nor its dried film indicates the presence of chirality in the structure by using the conventional techniques. In contrast, both the CNC/Salt and CNC/PEG systems display the characteristic texture of a CN* structure from suspension which is maintained in the dried film, as observed by SAXS, POM and SEM imaging.

After extensive water dialysis, most of impurities and remnant ions were removed, and the suspension was left with negatively and highly charged CNC rods. As the water evaporates, the volume

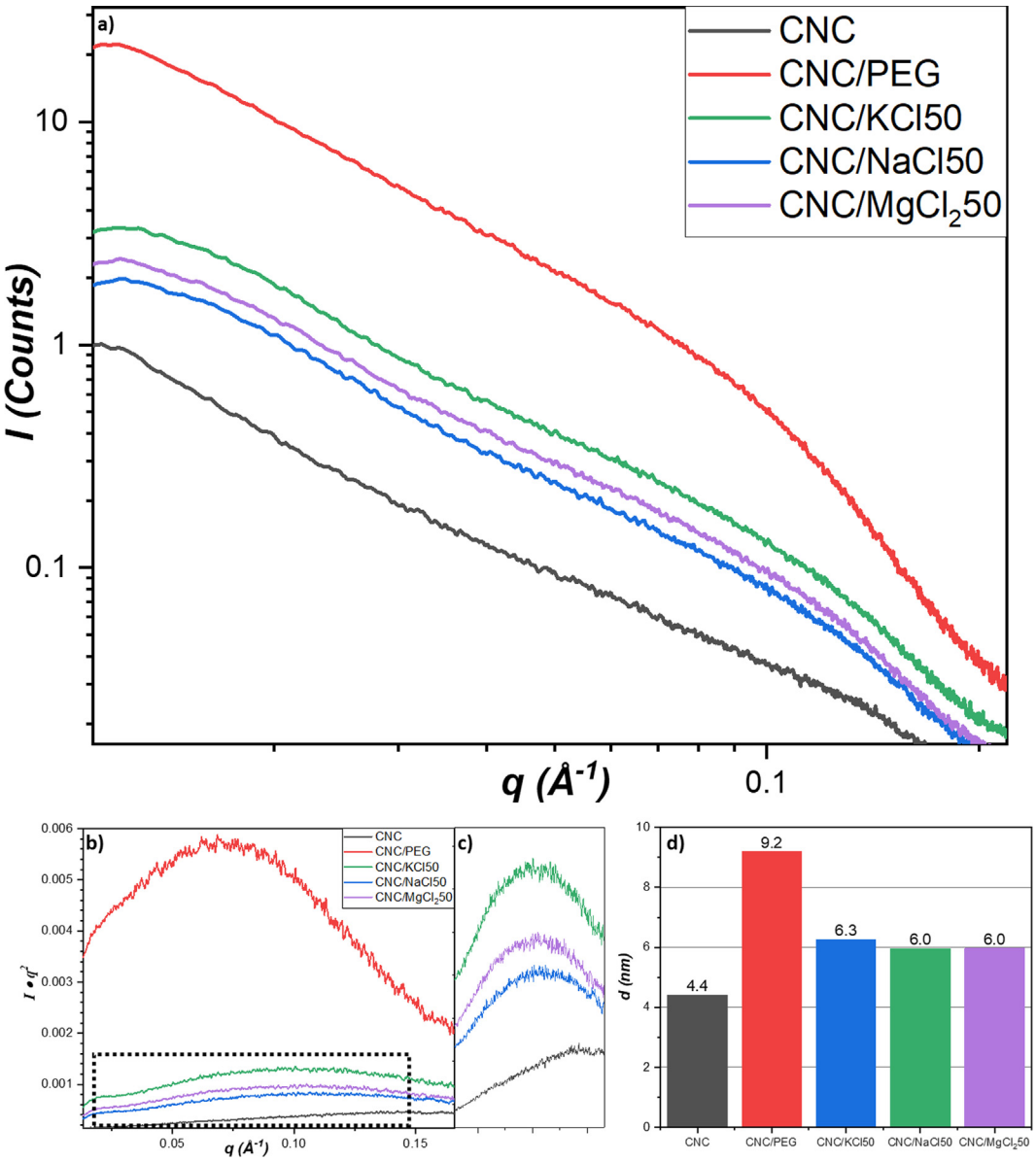

Fig. 6. The SAXS analysis of five typical CNC samples in the form of solid dried film. a) is original SAXS intensity-q vector curve and b) is its corresponding Kratky plot. c) The magnified figure of the area marked by square with square-dot perimeter shows the peaks of CNC/salt more clearly. d) is the summary of ***d*** calculated by Eq.(2).

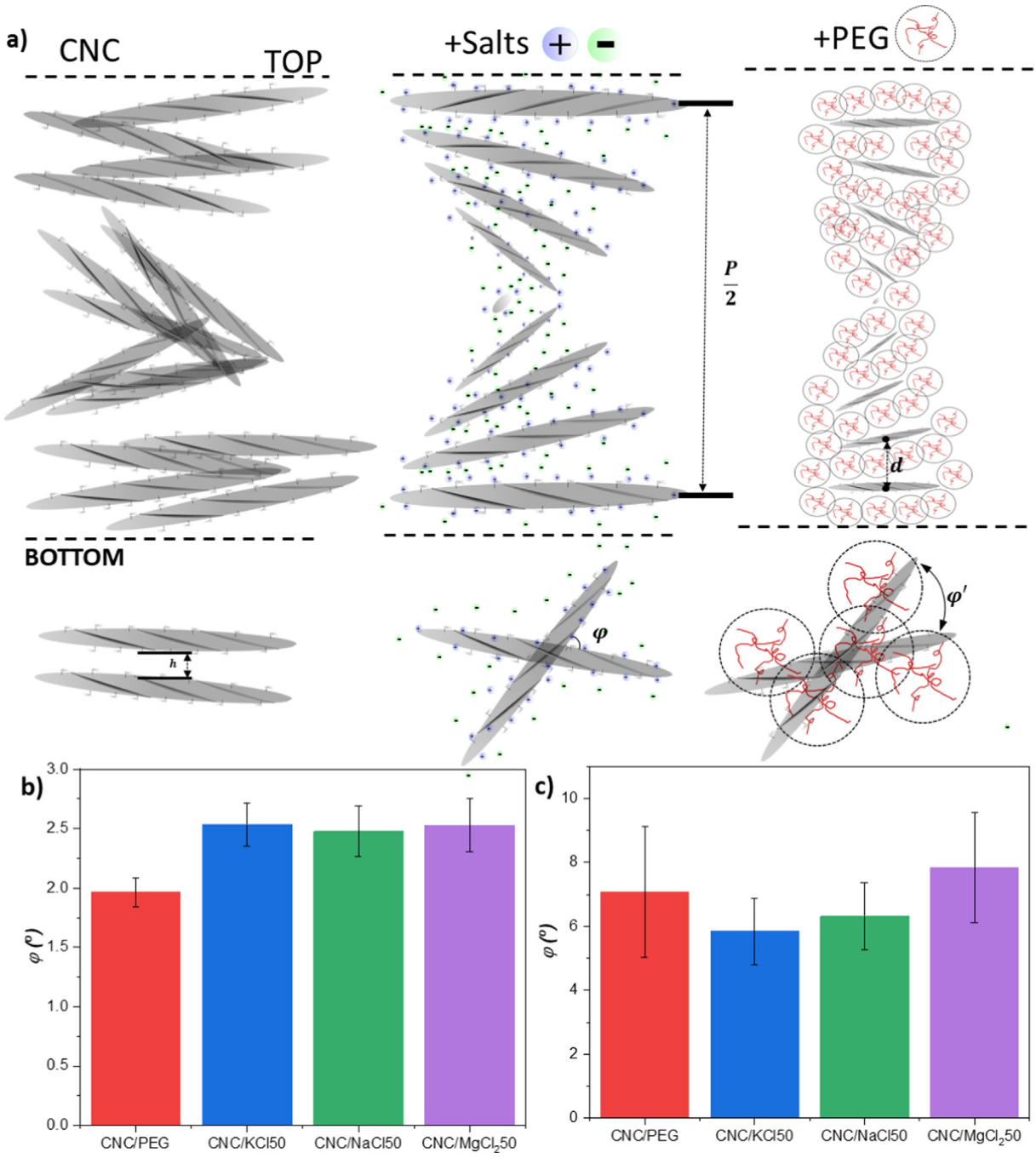

Fig. 7. a) Schematic representation of the structure and mechanisms driven the three systems: CNC, CNC/PEG and CNC/Salt suspensions. In neat system, CNC rods grouped in an achiral nematic way. After addition of salt or PEG, CNC rods start to form a chiral nematic structure with an interaxial angle φ. Summary of calculated interaxial angle φ occurring in b) all suspensions and c) all solid dried films (except CNC alone, as no CN*structure was formed in this instance).

of suspensions shrinks and the particle interaxial distance decreases due to the motion of the retreating air–water interface and capillary attraction [43]. With the high extent of electrostatic repulsive force and their high aspect ratio, the CNC rods assemble into a chiral nematic structure, as reported by POM in Fig. 2(a). Nematic CNC domains become disoriented, and the structures irregular, as illustrated in Fig. 7(a) when the suspension is fully dried. This is due to repulsive forces and observed as:1) the layered-like without the "Bouligand" structures evident in SEM (Fig. 4(b)) and 2), much reduced intensity at low q region with the flat SAXS curve in Fig. 6(c).

In all CNC/Salt systems, the suspensions show a biphasic state from POM (Fig. 2), while solid dried films consisted of CN* structures that are visualized by SEM in Fig. 5(a-i). Both d and P decreased when CNC/salt suspensions were dried into films. One factor determining the chirality of CN* structures is the interaxial angle φ between CNC rods as shown in Fig. 7(a). φ is calculated based on the following equation [44]:

$$\varphi = 360^{\circ} \cdot d/P \tag{4}$$

The values of φ from the various suspensions and dried films are summarized in Fig. 7 (b) and (c), respectively. With regards to ion types, the difference of φ between each suspension is small, while there is a significant difference in value between their solid films. The degree of ion adsorption on CNC was found to be

dependent on the type of ions [24]. For example, both Na^+ and K^+ are monovalent ions but the values of φ are different. Moreover, the interaxial angle can be affected by the suspension ionic strength. For the same concentration of salt, the ionic strength of $MgCl_2$ is the largest, $I_{MgCl_2} = 1.5I_{KCl} = 1.5I_{NaCl}$, based on Eq.(5):

$$\boldsymbol{I} = \frac{1}{2}\sum_{i=1}^{n} c_i z_i^2 \tag{5}$$

where c_i is molar concentration of an ion and z_i is the charge number of that ion[45]. In Fig. 2(c)-(e), the volume fraction of the CN* phase in CNC/$MgCl_2$ systems is larger than for CNC/KCl50 and CNC/NaCl50. Although three types of systems have similar $\boldsymbol{d}$ in dried film, φ increases with $\boldsymbol{I}$.

Structural differences between the neat CNC system and the CNC/salt ones can be related to different interaction energies between CNC rods. The interaction energy of CNC/Salt systems can be calculated from the Derjaguin-Landau-Verwey-Overbeek (DLVO) theory [46]. Examples relating to the two extreme scenarios of which neighbor CNC rods align in parallel and crossed forms are plotted in Fig.S1(a-b) in (**S.I.**). When CNC rods are aligned in a parallel fashion, as the salt concentration increases due to evaporation, a minimum interaction energy appears at an interaxial distance below 5 nm. This minimum forms an energy barrier which prevents CNCs packing closer. When CNC rods reorient into crossed forms, the minimum has a smaller value and is located at a smaller interaxial distance. The purpose of the interaxial angle and resultant chirality is to reduce the energy barrier so that CNCs can be as closely packed as possible. An equilibrium angle is attained driven by the balance of these two forces when the interaction area is sufficiently reduced, leading to a diminished electrostatic repulsion between the ends of the CNC rods. However, quantitively determining the interaction energy of CNC systems is challenging, since there are few calculations describing hard-rods interactions without salts or ions in water. Xue et al. proposed a method to calculate the Debye length by considering CNC as a polyelectrolyte and hydrogen ions as the counterion[20]. Although CNC rods are hard rods which are insoluble in water (unlike polyelectrolytes), most of the ions are excluded in our system and the actual repulsion is stronger. Thus, no minimum at low $\boldsymbol{d}$ based on the trend in Fig. S1(a) is observed, as shown in (**S.I.**). Further analysis is needed to create a better model for a hard rod system in a suspension without ions.

The CNC/PEG system displays a CN* structure in suspension as revealed by POM. Solid films of vivid iridescent color are visible by naked eye and the characteristic CN* microstructure is revealed by SEM. A depletion effects for PEG at this concentration (30 wt% in the dried film) and this MW (900,000 Da) was found in our previous study [31]. The intercalation of PEG molecules between the CNC crystals introduces an additional attractive force during mixing of the suspension. As a result, PEG forms a layer covering CNCs in the dried film, with a smaller $\boldsymbol{d}$ in suspension (Fig. 3(c)). This additional attraction changes the balance of forces in the gap and between the ends of the rod, which allows neighbor rods to rotate with an angle $\boldsymbol{\varphi}$**.** The reason it has the smallest φ of all suspensions may be related to the interaction energy. Based on Fig.S1, lowering the interaction energy caused by a depletion interaction can reduce the interaxial angle. However, reducing significantly the interaxial angle raises the electrostatic repulsion component. Consequently, a new equilibrium is reached between these two forces. The decrease in zeta-potential in Table.1 (from −69.8 mV to −52.7 mV) also implies this layer is not only acting physically as a "barrier" between CNC particles to weaken the interaction [31,47,48], but also it acts like a "Faraday cage", blocking the effect of the electric field generated by the surface potential of a CNC rod. From Fig. 7(a) and (b), the φ of CNC/PEG system also increases from 1.96° ± 0.12° to 7.09° ± 2.05° during evaporation. The CNC/PEG system may be similar to the CNC/salt system, of which neighbor CNC rods twist with an increasing φ to reduce the scale of energy minimum. This study analyzed the driving factor twisting neighbor CNCs in both CNC/salt and CNC/PEG systems. Although it is suspected that the handedness is related to the inherent chirality of cellulose molecules [49,50],the mechanism for the long-range order is still unclear.

5. Conclusion

The modulation of chirality for CNC assembly from suspension to solid dried film was achieved by the addition of salt and PEG. Zeta-potential measurements and SAXS were used to study the interaction between CNC particles. POM and SEM probe microstructures in liquid and solid, respectively. Reflectance UV–vis spectrometer allowed a full characterization of wavelength from 200 nm to 1000 nm of dried films.

Dilute CNC suspensions treated by a long-term water dialysis to remove counterions show a large zeta-potential value and achiral nematic behaviors. When this CNC suspension was dried into a solid film, no iridescent color is observed, and no peak occurs in its UV–vis spectrum. Previously, studies relied on the counterions generated during CNC extraction to produce CNC chiral nematic iridescent films [9–13,44]. In this study, by adding salts or PEG into the counterions free CNC suspension in controlled manner, the chirality of nematic structure occurs. By identifying peak position in the SAXS curves, the interaxial distances between CNC rods were calculated [44] to be smaller in salt (44.0 nm – 47.1 nm) and PEG (45.6 nm) systems compared to original neat system (48.7 nm). The CN* structure is preserved during drying with decreasing pitch size, decreasing interaxial distance and increasing interaxial angle of neighboring CNC particles, and the corresponding films show iridescence.

By considering CNC suspension as an ion-free media and relating the findings to the DLVO theory [17,20,46], the repulsive forces between CNC rods are too large to allow CNCs alone to assemble into a chiral structure. The addition of salts and PEG can reduce the repulsion by screening the surface charges and steric effect, respectively. We propose that chirality may rely on an equilibrium between repulsive and attractive forces and require an energy minimum. This work seeks to provide a deeper understanding of the mechanisms and factors behind CNC self-assembly.

CRediT authorship contribution statement

Maoqi Lin: Conceptualization, Methodology, Writing – original draft, Visualization, Formal analysis. **Vikram Singh Raghuwanshi:** Validation, Software, Writing – review & editing, Formal analysis. **Christine Browne:** Validation, Investigation, Writing – review & editing, Formal analysis. **George P Simon:** Writing – review & editing, Supervision, Project administration, Resources. **Gil Garnier:** Writing – review & editing, Supervision, Project administration, Funding acquisition, Resources.

Declaration of Competing Interest

The authors declare that they have no known competing financial interests or personal relationships that could have appeared to influence the work reported in this paper.

Acknowledgement

This work was supported by the funding from Australian Research Council, and our industry partners: Visy, Norske Skog, Opal – Industry Transformation Research Hub; Processing

Advanced Lignocellulosic (PALS) [Grant Number IH170100020]. The authors acknowledge SEM support from Monash Centre for Electron Microscope, Monash University (Clayton), size exclusion chromatography support from Dr. Sepa Nanayakkara, Chemistry, Monash University. The authors thank to the SAXS/WAXS(Synchrotron) beamline measuring suspensions support and beam time from the Australian Nuclear Science and Technology Organization (ANSTO) and SAXS at the Monash X-ray platform, Monash University (Clayton).

Appendix A. Supplementary material

Supplementary data to this article can be found online at https://doi.org/10.1016/j.jcis.2021.12.182.

References

[1] A. Narkevicius, L.M. Steiner, R.M. Parker, Y.u. Ogawa, B. Frka-Petesic, S. Vignolini, Controlling the Self-Assembly Behavior of Aqueous Chitin Nanocrystal Suspensions, Biomacromolecules 20 (7) (2019) 2830–2838.
[2] J.J. Kaschuk, Y.A. Haj, O.J. Rojas, K. Miettunen, T. Abitbol, J. Vapaavuori, Plant-based Structures as an Opportunity to Engineer Optical Functions in next-generation Light Management, Adv. Mater. 2104473 (2021).
[3] Y. Habibi, L.A. Lucia, O.J. Rojas, Cellulose Nanocrystals: Chemistry, Self-Assembly, and Applications, Chem. Rev. 110 (6) (2010) 3479–3500.
[4] Z. Zhang, G. Sèbe, X. Wang, K.C. Tam, UV-Absorbing Cellulose Nanocrystals as Functional Reinforcing Fillers in Poly(vinyl chloride) Films, ACS Appl. Nano Mater. 1 (2) (2018) 632–641.
[5] Y. Yin, J. Ma, X. Tian, X. Jiang, H. Wang, W. Gao, Cellulose nanocrystals functionalized with amino-silane and epoxy-poly(ethylene glycol) for reinforcement and flexibilization of poly(lactic acid): material preparation and compatibility mechanism, Cellulose 25 (11) (2018) 6447–6463.
[6] M. Giese, M. Spengler, Cellulose nanocrystals in nanoarchitectonics towards photonic functional materials, Mol. Syst. Des. Eng. 4 (1) (2019) 29–48.
[7] Y.-D. He, Z.-L. Zhang, J. Xue, X.-H. Wang, F. Song, X.-L. Wang, L.-L. Zhu, Y.-Z. Wang, Biomimetic Optical Cellulose Nanocrystal Films with Controllable Iridescent Color and Environmental Stimuli-Responsive Chromism, ACS Appl. Mater. Interfaces 10 (6) (2018) 5805–5811.
[8] R. Bardet, N. Belgacem, J. Bras, Flexibility and color monitoring of cellulose nanocrystal iridescent solid films using anionic or neutral polymers, ACS Appl. Mater. Interfaces 7 (7) (2015) 4010–4018.
[9] X. Mu, D.G. Gray, Droplets of cellulose nanocrystal suspensions on drying give iridescent 3-D "coffee-stain" rings, Cellulose 22 (2) (2015) 1103–1107.
[10] D.G. Gray, Recent Advances in Chiral Nematic Structure and Iridescent Color of Cellulose Nanocrystal Films, Nanomaterials 6 (11) (2016) 213.
[11] G. Picard, D. Simon, Y. Kadiri, J.D. LeBreux, F. Ghozayel, Cellulose Nanocrystal Iridescence: A New Model, Langmuir 28 (41) (2012) 14799–14807.
[12] A. Gençer, C. Schütz, W. Thielemans, Influence of the Particle Concentration and Marangoni Flow on the Formation of Cellulose Nanocrystal Films, Langmuir 33 (1) (2017) 228–234.
[13] D. Liu, S. Wang, Z. Ma, D. Tian, M. Gu, F. Lin, Structurecolor mechanism of iridescent cellulose nanocrystal films, RSC Adv. 4 (74) (2014) 39322–39331.
[14] H. Oguzlu, C. Danumah, Y. Boluk, Colloidal behavior of aqueous cellulose nanocrystal suspensions, Curr. Opin. Colloid Interface Sci. 29 (2017) 46–56.
[15] R.M. Parker, G. Guidetti, C.A. Williams, T. Zhao, A. Narkevicius, S. Vignolini, B. Frka-Petesic, The Self-Assembly of Cellulose Nanocrystals: Hierarchical Design of Visual Appearance, Adv. Mater. 30 (19) (2018) 1704477.
[16] B. Frka-Petesic, J.A. Kelly, G. Jacucci, G. Guidetti, G. Kamita, N.P. Crossette, W.Y. Hamad, M.J. MacLachlan, S. Vignolini, Retrieving the Coassembly Pathway of Composite Cellulose Nanocrystal Photonic Films from their Angular Optical Response, Adv. Mater. 32 (19) (2020) 1906889, https://doi.org/10.1002/adma.201906889.
[17] M.S. Reid, S.A. Kedzior, M. Villalobos, E.D. Cranston, Effect of Ionic Strength and Surface Charge Density on the Kinetics of Cellulose Nanocrystal Thin Film Swelling, Langmuir 33 (30) (2017) 7403–7411.
[18] P. Liu, X. Guo, F. Nan, Y. Duan, J. Zhang, Modifying Mechanical, Optical Properties and Thermal Processability of Iridescent Cellulose Nanocrystal Films Using Ionic Liquid, ACS Appl. Mater. Interfaces 9 (3) (2017) 3085–3092.
[19] X.M. Dong, T. Kimura, J.-F. Revol, D.G. Gray, Effects of Ionic Strength on the Isotropic–Chiral Nematic Phase Transition of Suspensions of Cellulose Crystallites, Langmuir 12 (8) (1996) 2076–2082.
[20] X.M. Dong, D.G. Gray, Effect of Counterions on Ordered Phase Formation in Suspensions of Charged Rodlike Cellulose Crystallites, Langmuir 13 (8) (1997) 2404–2409.
[21] F. Cherhal, F. Cousin, I. Capron, Influence of Charge Density and Ionic Strength on the Aggregation Process of Cellulose Nanocrystals in Aqueous Suspension, as Revealed by Small-Angle Neutron Scattering, Langmuir 31 (20) (2015) 5596–5602.
[22] T. Phan-Xuan, A. Thuresson, M. Skepö, A. Labrador, R. Bordes, A. Matic, Aggregation behavior of aqueous cellulose nanocrystals: the effect of inorganic salts, Cellulose 23 (6) (2016) 3653–3663.
[23] T. Cao, M. Elimelech, Colloidal stability of cellulose nanocrystals in aqueous solutions containing monovalent, divalent, and trivalent inorganic salts, J. Colloid Interface Sci. 584 (2021) 456–463.
[24] R. Prathapan, R. Thapa, G. Garnier, R.F. Tabor, Modulating the zeta potential of cellulose nanocrystals using salts and surfactants, Colloids Surf., A 509 (C) (2016) 11–18.
[25] S. Lombardo, A. Gençer, C. Schütz, J. Van Rie, S. Eyley, W. Thielemans, Thermodynamic Study of Ion-Driven Aggregation of Cellulose Nanocrystals, Biomacromolecules 20 (8) (2019) 3181–3190.
[26] Y. Wang, Z. Chen, J. Tang, N. Lin, Tunable Optical Materials Based on Self-assembly of Polysaccharide Nanocrystals, in: N. Lin, J. Tang, A. Dufresne, M.K. C. Tam (Eds.), Advanced Functional Materials from Nanopolysaccharides, Springer Singapore, Singapore, 2019, pp. 87–136.
[27] Y.u. Zhang, Z. Tian, Y. Fu, Z. Wang, M. Qin, Z. Yuan, Responsive and patterned cellulose nanocrystal films modified by N-methylmorpholine-N-oxide, Carbohydr. Polym. 228 (2020) 115387, https://doi.org/10.1016/j.carbpol.2019.115387.
[28] O. Kose, A. Tran, L. Lewis, W.Y. Hamad, M.J. MacLachlan, Unwinding a spiral of cellulose nanocrystals for stimuli-responsive stretchable optics, Nat. Commun. 10 (1) (2019) 1–7.
[29] Y.P. Zhang, V.P. Chodavarapu, A.G. Kirk, M.P. Andrews, Nanocrystalline cellulose for covert optical encryption, J. Nanophotonics 6 (1) (2012) 063516.
[30] M.S. Reid, M. Villalobos, E.D. Cranston, The role of hydrogen bonding in non-ionic polymer adsorption to cellulose nanocrystals and silica colloids, Curr. Opin. Colloid Interface Sci. 29 (2017) 76–82.
[31] M. Lin, V.S. Raghuwanshi, C. Browne, G.P. Simon, G. Garnier, Modulating transparency and colour of cellulose nanocrystal composite films by varying polymer molecular weight, J. Colloid Interface Sci. 584 (2021) 216–224.
[32] A. Sze, D. Erickson, L. Ren, D. Li, Zeta-potential measurement using the Smoluchowski equation and the slope of the current–time relationship in electroosmotic flow, J. Colloid Interface Sci. 261 (2) (2003) 402–410.
[33] V. Cherpak, V.F. Korolovych, R. Geryak, T. Turiv, D. Nepal, J. Kelly, T.J. Bunning, O.D. Lavrentovich, W.T. Heller, V.V. Tsukruk, Robust Chiral Organization of Cellulose Nanocrystals in Capillary Confinement, Nano Lett. 18 (11) (2018) 6770–6777.
[34] K.C. Majumdar, N. Pal, S. Nath, S. Choudhury, N.V.S. Rao, Synthesis, Characterization, and Mesogenic Properties of Anisotropic Imines, Mol. Cryst. Liq. Cryst. 461 (1) (2006) 37–51.
[35] X. Mu, D.G. Gray, Formation of chiral nematic films from cellulose nanocrystal suspensions is a two-stage process, Langmuir : the ACS journal of surfaces and colloids 30 (31) (2014) 9256.
[36] J.P.F. Lagerwall, C. Schütz, M. Salajkova, JungHyun Noh, J.i. Hyun Park, G. Scalia, L. Bergström, Cellulose nanocrystal-based materials: from liquid crystal self-assembly and glass formation to multifunctional thin films, NPG Asia Mater. 6 (1) (2014) e80.
[37] A.G. Dumanli, H.M. van der Kooij, G. Kamita, E. Reisner, J.J. Baumberg, U. Steiner, S. Vignolini, Digital Color in Cellulose Nanocrystal Films, ACS Appl. Mater. Interfaces 6 (15) (2014) 12302–12306.
[38] L.M. Anovitz, X. Zhang, J. Soltis, E. Nakouzi, A.J. Krzysko, J. Chun, G.K. Schenter, T.R. Graham, K.M. Rosso, J.J. De Yoreo, A.G. Stack, M. Bleuel, C. Gagnon, D.F.R. Mildner, J. Ilavsky, I. Kuzmenko, Effects of Ionic Strength, Salt, and pH on Aggregation of Boehmite Nanocrystals: Tumbler Small-Angle Neutron and X-ray Scattering and Imaging Analysis, Langmuir 34 (51) (2018) 15839–15853.
[39] P.U. Sastry, D.P. Dutta, Fractal characteristics of nanocrystalline indium and gallium sulfide particles, J. Alloy. Compd. 487 (1-2) (2009) 351–353.
[40] B. Frka-Petesic, G. Kamita, G. Guidetti, S. Vignolini, Angular optical response of cellulose nanocrystal films explained by the distortion of the arrested suspension upon drying, Phys. Rev. Mater. 3 (4) (2019) 045601.
[41] N. Bumbudsanpharoke, S. Kwon, W. Lee, S. Ko, Optical response of photonic cellulose nanocrystal film for a novel humidity indicator, Int. J. Biol. Macromol. 140 (2019) 91–97.
[42] C.C.Y. Cheung, M. Giese, J.A. Kelly, W.Y. Hamad, M.J. MacLachlan, Iridescent Chiral Nematic Cellulose Nanocrystal/Polymer Composites Assembled in Organic Solvents, ACS Macro Lett. 2 (11) (2013) 1016–1020.
[43] M.-J. Dalbe, D. Cosic, M. Berhanu, A. Kudrolli, Aggregation of frictional particles due to capillary attraction, Phys. Rev. E 83 (5) (2011) 051403.
[44] C. Schütz, M. Agthe, A.B. Fall, K. Gordeyeva, V. Guccini, M. Salajková, T.S. Plivelic, J.P.F. Lagerwall, G. Salazar-Alvarez, L. Bergström, Rod Packing in Chiral Nematic Cellulose Nanocrystal Dispersions Studied by Small-Angle X-ray Scattering and Laser Diffraction, Langmuir 31 (23) (2015) 6507–6513.
[45] S.M. Truscott, Chapter 6 - Laboratory calculations, in: W. Clarke, M.A. Marzinke (Eds.), Contemporary Practice in Clinical Chemistry (Fourth Edition), Academic Press, 2020, pp. 97–117.
[46] J.N. Israelachvili, Intermolecular and Surface Forces (3rd Edition), Elsevier.
[47] H. Oguzlu, Y. Boluk, Interactions between cellulose nanocrystals and anionic and neutral polymers in aqueous solutions, Cellulose 24 (1) (2017) 131–146.
[48] D. Cheng, Y. Wen, L. Wang, X. An, X. Zhu, Y. Ni, Adsorption of polyethylene glycol (PEG) onto cellulose nano-crystals to improve its dispersity, Carbohydr. Polym. 123 (2015) 157–163.
[49] S.N. Fernandes, P.L. Almeida, N. Monge, L.E. Aguirre, D. Reis, C.L.P. de Oliveira, A.M.F. Neto, P. Pieranski, M.H. Godinho, Mind the Microgap in Iridescent Cellulose Nanocrystal Films, Adv. Mater. 29 (2) (2017) 1603560.
[50] J. Majoinen, E. Kontturi, O. Ikkala, D.G. Gray, SEM imaging of chiral nematic films cast from cellulose nanocrystal suspensions, Cellulose 19 (5) (2012) 1599–1605.